



## NUMERICAL STUDY OF MILITARY AIRFOILS DESIGN FOR COMPRESSIBLE FLOW

Aslam Abdullah, Muhamad Nabil Sabhi Mohd Jafri and Mohd Fadhi Zulkafli  
 Department of Aeronautical Engineering, Faculty of Mechanical and Manufacturing Engineering,  
 Universiti Tun Hussein Onn Malaysia, Parit Raja, Batu Pahat, Johor, Malaysia  
 E-Mail: [aslam@uthm.edu.my](mailto:aslam@uthm.edu.my)

### ABSTRACT

The paper presents an aerodynamic analysis of compressible flow over airfoils used in the wing design of several military aircrafts. The calculations involved solving FANS equations. The influence of angle of attack on lifts and drags for all airfoils of interest were examined. The velocity contours were also analyzed and the onset of flow separation prior to stall was successfully determined. Furthermore, the aerodynamics data were classified as belong to either cambered or un-cambered airfoils.

**Keywords:** aerodynamic analysis, compressible flow, NACA airfoils, and military airfoils.

### 1. INTRODUCTION

Back in 1884, the earliest patented airfoil shape was established by Horatio F. Philips [1]. Since then many airfoil designs are available especially for study in various classes of aircrafts, ranging from pioneered 1-series [2] to supercritical 8-series airfoils [3], and from rounded leading edge subsonic [4,5] to biconvex supersonic airfoils [6].

While it is reasonably acceptable to learn their low speed incompressible aerodynamics as, for instance, in [7-9], the findings are not straightforwardly applicable to most of the flight envelopes due to the nature of airflow that is compressible. This study aims not only to contribute to the compressible aerodynamic data for airfoils of interest in order to complement those for incompressible flow, but also compare the outputs.

The compressibility effect of the external airflow becomes apparent when Mach number  $M > 0.3$ , and needs to be taken into consideration in the calculation of aerodynamic properties. Compressible flows can be classified into subsonic, supersonic and hypersonic, based on Mach number [10].

The paper compares the aerodynamic performance of the airfoils in compressible subsonic flow where  $0.3 < M < 1$ . A steady-state Favre-averaged Navier-Stokes (FANS) investigation was performed using the commercial CFD code ANSYS. The wing cross-sections were divided into symmetrical or un-cambered (i.e. NACA 0003 and NACA 0012) and asymmetrical or cambered airfoils (i.e. NACA 64-206 and NACA 64-210). The characteristics of flow over four airfoils of interest were evaluated. The airfoils form the cross sections of military airplanes [11] as shown in Table-1. The specifications of the individual airplane can be found in [12-15].

The comparison for both types of airfoil should fall within the scope of the fundamental airfoil theories such as in the case of the lift and drag production versus angle of attack  $\alpha$  as well as the critical or stall angle of attack  $\alpha_c$  beyond which the lift degrades [16].

**Table-1.** Airfoils of interest and their corresponding military airplanes.

Airfoil series	Military airplane
NACA 0003	McDonnell Douglas F-4 Phantom II
NACA 0012	Lockheed S-3 Viking
NACA 64-206	General Dynamics F-16 Fighting Falcon
NACA 64-210	General Dynamics F-111 Aardvark

### 2. GOVERNING EQUATIONS AND MODELLING ASSUMPTIONS

A finite volume numerical method based on solving FANS equations describing the case under consideration was used for calculating the flow around the airfoil. We first present full Navier-Stokes equations in conservation form for viscous compressible flow as

$$\frac{\partial \rho}{\partial t} + \frac{\partial}{\partial x_m} (\rho u_m) = 0, \quad (1)$$

$$\frac{\partial}{\partial t} (\rho u_m) + \frac{\partial}{\partial x_n} (\rho u_n u_m) = 0, \quad (2)$$

and

$$\begin{aligned} & \frac{\partial}{\partial t} \left[ \rho \left( e + \frac{u_m u_m}{2} \right) \right] + \frac{\partial}{\partial x_n} \left[ \rho u_n \left( h + \frac{u_m u_m}{2} \right) \right] \\ & = \frac{\partial}{\partial x_n} (u_n \tau_{mn}) - \frac{\partial q_n}{\partial x_n}, \end{aligned} \quad (3)$$

where  $\rho$  is density,  $u_k$  is velocity,  $e$  is specific internal energy,  $h$  is specific enthalpy,  $\tau_{mn}$  is viscous stress tensor, and  $q_n$  is heat flux vector. Note that  $h = e + p/\rho$ ,  $\tau_{mn} = 2\mu \left( s_{mn} - \frac{1}{3} \frac{\partial u_k}{\partial x_k} \delta_{mn} \right)$ , and  $q_n = -\gamma \frac{\partial T}{\partial x_n}$ , where  $s_{mn}$  is strain-rate tensor given by  $s_{mn} =$



$\frac{1}{2} \left( \frac{\partial u_m}{\partial x_n} + \frac{\partial u_n}{\partial x_m} \right)$ ,  $\gamma$  is thermal conductivity, and  $T$  is temperature.

For turbulent flow, the Reynolds decomposition for  $\rho$ ,  $\rho$ , and  $q$  as Favre decomposition for  $u$ ,  $h$ , and  $e$  are first defined as

$$\rho = \bar{\rho} + \rho', \quad \rho = \bar{\rho} + \rho', \quad q = \bar{q} + q' \quad (4)$$

$$u_k = \tilde{u}_k + u_k'', \quad h = \tilde{h} + h'', \quad e = \tilde{e} + e'' \quad (5)$$

Substituting Equations. (4) and (5) into Equations. (1)-(3), taking the time average and assuming steady state flow, we have

$$\frac{\partial}{\partial x_m} (\bar{\rho} \tilde{u}_m) = 0, \quad (6)$$

$$\frac{\partial (\bar{\rho} \tilde{u}_m \tilde{u}_n)}{\partial x_n} = -\frac{\partial \bar{p}}{\partial x_m} + \frac{\partial \bar{\tau}_{mn}}{\partial x_n} - \frac{\partial}{\partial x_n} (\overline{\rho u_m'' u_n''}), \quad (7)$$

and

$$\begin{aligned} & \frac{\partial}{\partial t} \left[ \bar{\rho} \left( \tilde{e} + \frac{\tilde{u}_m \tilde{u}_m}{2} \right) + \frac{\overline{\rho u_m'' u_m''}}{2} \right] \\ & + \frac{\partial}{\partial x_n} \left[ \bar{\rho} \tilde{u}_n \left( \tilde{h} + \frac{\tilde{u}_m \tilde{u}_m}{2} \right) + \tilde{u}_n \frac{\overline{\rho u_m'' u_m''}}{2} \right] \\ & = \frac{\partial}{\partial x_n} \left[ \tilde{u}_m (\bar{\tau}_{mn} - \overline{\rho u_m'' u_n''}) - \bar{q} - \overline{\rho u_n'' h''} \right. \\ & \left. + \overline{\tau_{nm} u_m''} - \overline{\rho u_n'' \frac{1}{2} u_m'' u_m''} \right]. \quad (8) \end{aligned}$$

It is necessary that the continuity Equation. (6) is satisfied by Equations. (7) and (8). Since the Reynolds averaging is involved in the derivation of Equations. (6)-(8), then a set of new unknowns called the Reynolds stresses  $-\overline{\rho u_m'' u_n''}$  appear. Note that these stresses are symmetric tensors such that  $-\overline{\rho u_m'' u_n''} = -\overline{\rho u_n'' u_m''}$ , and need to be modelled to ensure that the equations can be closed. In particular, the SSTk- $\omega$  turbulence model which gives a general description of turbulence by means of two transport equations was chosen.

The method was applied with second-order upwind discretization schemes for (6)-(8) as well as the SST k- $\omega$  turbulence model equations [17]. The density-based solver was employed to solve the governing equations of continuity, momentum and energy (6)-(8) simultaneously (i.e. these equations were coupled together). Afterward and sequentially the turbulence model equations were solved where each equation was segregated from one another and from the coupled set.

The airfoil velocity and the Reynolds number are 236 m/s and  $12 \times 10^6$ , respectively. The Mach number of flow is 0.7, so then the compressibility effects could not be neglected. Various angles of attack  $\alpha$  for different airfoil

geometries were considered for the investigation of the corresponding flow characteristics.

### 3. GEOMETRY, GRID AND COMPUTATIONAL DOMAIN

The flow of interest is that over the NACA 0003, NACA 0012, NACA 64-206 and NACA 64-210 airfoils. Among these airfoils, NACA 0003 and NACA 64-206 are labelled here as thin airfoils based on their relative geometries given in Figure-1. The airfoil models in unbounded flow and the grid used for calculations are given in Figure-2.

For discretization of the computational domain, an unstructured type of grid with quad elements was selected. Inlet and outlet boundary conditions were specified on the outer sides of computational domain with necessary turbulence and flow parameters. The fact that there is no slip between the airfoil and the layer of air immediately adjacent to it necessitates the no-slip boundary condition of viscous flow enforcement where the velocity of the air at the surface of the airfoil is zero. This should produce better representation of the reversing flow assumption since its occurrence depends on such condition.

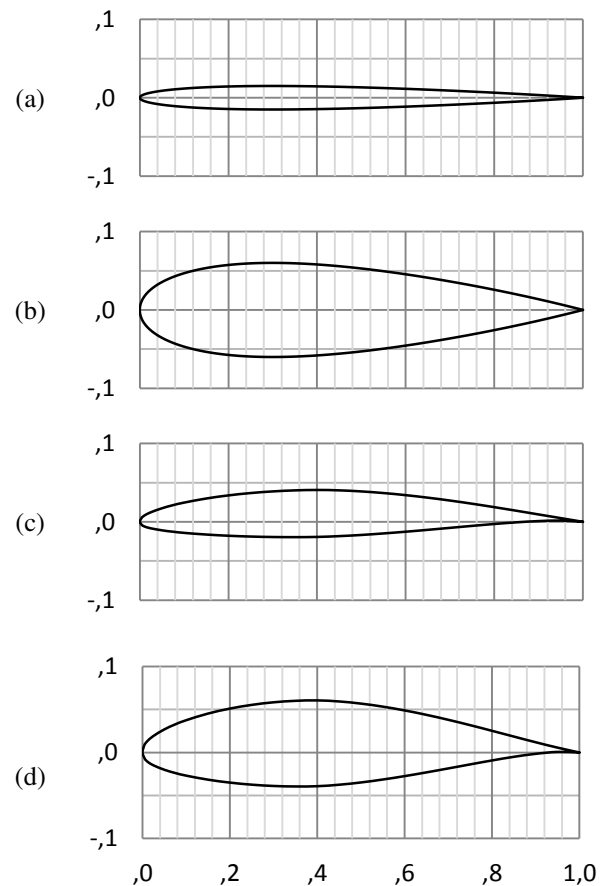
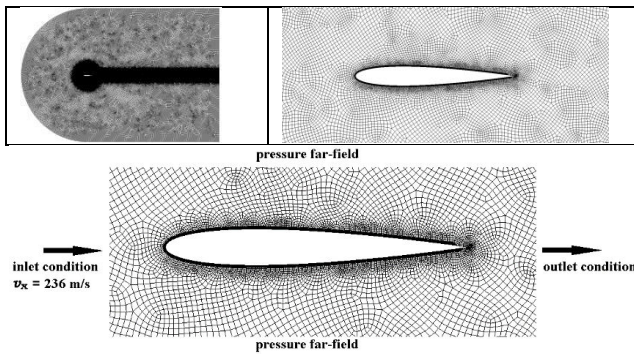


Figure-1. Geometry of airfoils (a) NACA 0003 (b) NACA 0012 (c) NACA 64-206 (d) NACA 64-210.



**Figure-2.** Grid applied for airfoil moving in unbounded flow.

**4. RESULTS OF CALCULATIONS**

Three types of results will be discussed, namely the velocity distribution as well as lift and drag profiles. The velocity fields around the airfoils at  $\alpha = \alpha_0 = 0$  and

$\alpha_c$  are shown in Figure-3. Note that these airfoils are in unbounded flow. It is obvious that a moment after reaching  $\alpha_c$  the induced velocity differences and thus the lifts are higher which directly influence L/D. In addition, the stagnation points shift from the leading edge at  $\alpha_0$  to the lower sides of the airfoils at  $\alpha_c$ . In contrast to the field contours in Figures 3(a)-3(b) at  $\alpha_0$ , those in Figure 3(c)-3(d) are unsymmetrical about the chord lines as expected for cambered airfoil geometries (i.e. NACA 64-206 and NACA 64-210).

The signs of flow separation also begin to emerge but are not yet fully developed at  $\alpha_c$ . The flow is most attached in the case of NACA 0012 (Figure-3(b)), followed by NACA 64-210 (Figure-3(d)), NACA 64-206 (Figure-3(c)) and NACA 0003 (Figure-3(a)). Further observation is necessary to relate the early sign of flow separation to  $\alpha_c$ .

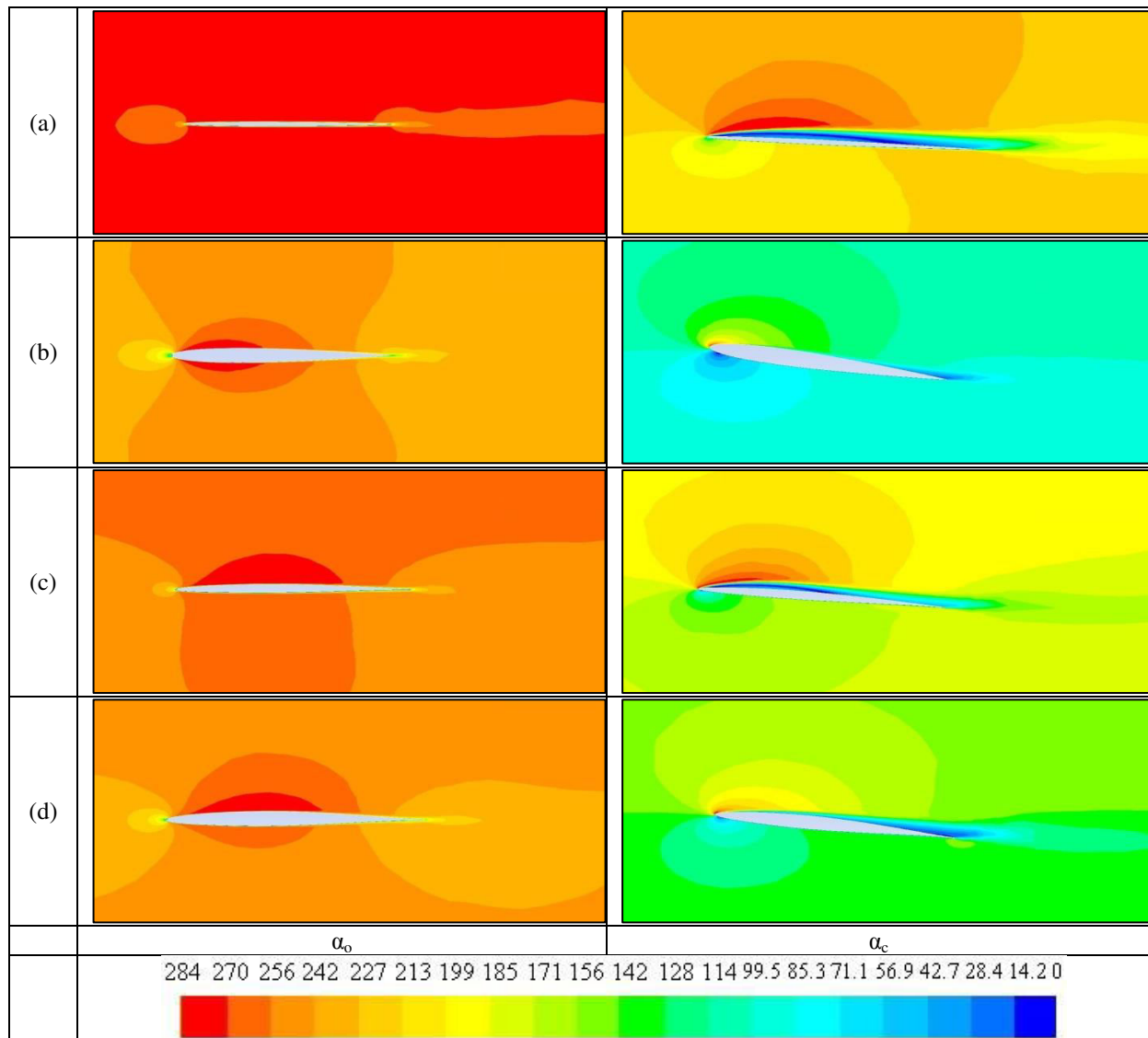


**Figure-3.** Velocity contour in m/s at  $\alpha_0$  and  $\alpha_c$  (a) NACA 0003 (b) NACA 0012 (c) NACA 64-206 (d) NACA 64-210.



Higher lift and more significant drop in lift past stall can be seen for both cambered NACA 64-206 and NACA 64-210 airfoils, while lower  $\alpha_c$  are found for thin NACA 0003 and NACA 64-206 airfoils (see Figure-4).

Sharp leading edge causes the airflow over the thin airfoils becomes more susceptible to flow separation, and thus leads to stall and a higher drag at lower angle of attack as can be seen in Figure-5. In addition, the thin airfoils promote more pronounced signs of flow separation at  $\alpha$  as suggested by Figures 3(a) and 3(c).

It is worth to note that despite the flow separation issue which accompanies the application of thin airfoils at low speed, fighter aircrafts equipped with powerful jet engine often use these types of airfoils to overcome the formation of a detached bow shock in front of the leading edge moving at supersonic speed. Better performance can be achieved by introducing high-lift devices such as virtual Gurney flaps that are able to delay the flow separation [18]. Other techniques include the flow separation control by means of plasma actuator and fiber Bragg grating (FBG) sensor located at specific locations on the airfoil surface [19]. Besides, the application of leading edge root extension (LERX) is very useful in generating more lift at subsonic speed and high angle of attack [20-22].

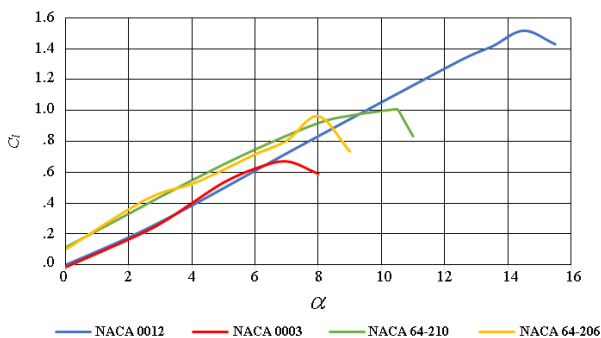


Figure-4. The lift coefficient  $C_l$  profiles.

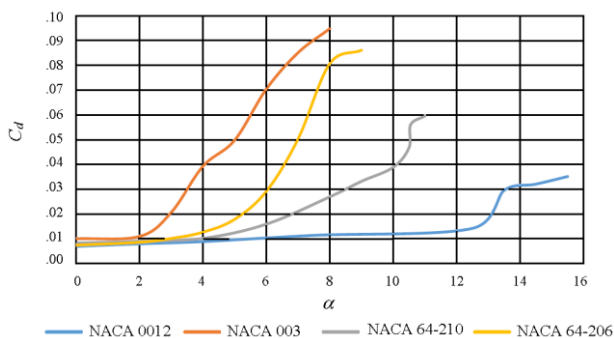


Figure-5. The drag coefficient  $C_d$  profiles.

## 5. FINAL REMARKS

The aerodynamic properties of four military airfoils, namely NACA 0003, NACA 0012, NACA 64-206 and NACA 64-210, have been studied. The main results can be summarized as follows:

As the stall angle of attack is reached, flow separation begins to take place. This is due to the pressure side of the airfoil that prevents the incoming air to flow smoothly through the top surface of the airfoil.

The difference in pressure across the asymmetrical airfoils (i.e. NACA 64-206 and NACA 64-210) produces higher lift than that across the symmetrical airfoils at a given angle of attack. However, the lifts drop off rapidly once stall angle of attack is reached.

The thinner airfoils (i.e. NACA 0003 and NACA 64-206) experience higher drags. Moreover, their stall angles of attack are smaller; sharp leading edges induce flow separations.

## ACKNOWLEDGEMENT

The author would like to thank Universiti Tun Hussein Onn Malaysia (UTHM) for providing financial support through IGSP Grant (VotU416).

## REFERENCES

- [1] Anderson J. D., Jr. 2001. Airfoil nomenclature. *Fundamental of Aerodynamics* 3<sup>rd</sup> Edition. New York: McGraw-Hill Higher Education. 278-281.
- [2] Pendley R. E. and Smith N. F. 1949. An investigation of the characteristics of three NACA 1-series nose inlets at subcritical and supercritical Mach numbers. *NACA Research Memorandum*. Washington: National Advisory Committee of Aeronautics. 1-38.
- [3] Whitcomb R. T. 1974. Review of NASA supercritical airfoils. *ICAS*. 74: 25-30.
- [4] McGhee R. J., Beasley W. D. and Whitcomb R. T. 1979. *NASA low-and medium-speed airfoil development*. NASA Technical Memorandum. Washington: National Aeronautics and Space Administration. 1-19.
- [5] Sahu N. K. and Imam, M. S. 2015. Analysis of transonic flow over an airfoil NACA 0012 using CFD. *IJISET*. 2: 379-388.
- [6] Hamid M. D., Hasan A. B. M. T., Alimuzzaman S. M., Matsuo S. and Setoguchi T. 2014. Compressible flow characteristics around a biconvex arc airfoil in a channel. *Propulsion and Power Research*. 3: 29-40.
- [7] Gad-el-Hak M. 1990. Control of low-speed airfoil aerodynamics. *AIAA Journal*. 28: 1537-1552.
- [8] Liebeck R. H. A. 1973. Class of airfoils designed for high lift in incompressible flow. *Journal of Aircraft*. 10: 610-617.



- [9] Rogers S. E., Wiltberger N. L. and Kwak D. 1993. Efficient simulation of incompressible viscous flow over single and multielement airfoils. *Journal of Aircraft*.30:736-743.
- [10] Rathakrishnan E. 2013. *Theoretical Aerodynamics*. Singapore: John Wiley & Sons Singapore Pte. Ltd.
- [11] Holmes T. 1998. *Jane's Historic Military Aircraft*. New York: HarperCollins.
- [12] Davis P. E. 2016. *USN McDonnell Douglas F-4 Phantom II*. Osprey Publishing.
- [13] Elward B. 2012. *S-3 Viking in Action*. Squadron/Signal Publication.
- [14] Davies S. 2014. *General Dynamics F-16 Fighting Falcon Manual*. UK: Haynes Publishing.
- [15] Davis P. E. 2013. *General Dynamics F-111 Aardvark*. Osprey Publishing.
- [16] Abbott I. H. and Doenhoff A. E. V. 1959. *Theory of Wing Sections*. New York: Dover Publications, Inc.
- [17] Wilcox D. C. 1993. A two-equation turbulence model for wall-bounded and free-shear flows. *AIAA 24th Fluid Dynamics Conference*.
- [18] Feng L., Choi K. and Wang J. 2015. Flow control over an airfoil using virtual Gurney flaps. *Journal of Fluid Mechanics*.767: 595-626.
- [19] Segawa T., Suzuki D., Fujino T., Jukes T. and Matsunuma T. 2016. Feedback control of flow separation using plasma actuator and FBG sensor. *International Journal of Aerospace Engineering*.
- [20] Adams R. J., Buffington J. M. and Banda S. S. 1994. Design of nonlinear control laws for high-angle-of-attack flight. *Journal of Guidance, Control, and Dynamics*.17: 737-746.
- [21] Buffington J., Adams R. and Banda S. 1993. Robust, nonlinear, high angle-of-attack control design for a super maneuverable vehicle. *Guidance, Navigation and Control Conference*. 3774.
- [22] Chung J. and Parikh P. C. A. 2003. Computational study of the abrupt wing stalls (AWS) characteristics for various fighter jets: part II, AV-8B& F/A-18C. *IEEE User Group Conference*.129-140.